RSC Advances

PAPER

Cite this: *RSC Adv.*, 2018, **8**, 27332

Luminescence properties and energy transfer investigations of $Ba_2La_{2.85-x}Tb_{0.15}Eu_x(SiO_4)_3F$ multicolor phosphor

Xiaoxue Ma,[a] Libing Liao, *[a] Qingfeng Guo,[b] Haikun Liu,[a] Tianshuai Zhou[a] and Lefu Mei*[a]

Received 28th May 2018
Accepted 13th July 2018

DOI: 10.1039/c8ra04534h

rsc.li/rsc-advances

The $Ba_2La_{2.85-x}Tb_{0.15}Eu_x(SiO_4)_3F$ (BLSOF:0.15Tb^{3+}, xEu^{3+}) multicolor phosphors with apatite structure were synthesized *via* the solid-state pathway. The crystal structure and luminescence properties of the phosphors were investigated by means of scanning electron microscopy (SEM), X-ray diffraction (XRD), Rietveld refinement, photoluminescence excitation (PLE) and photoluminescence (PL). The luminescence performance of the phosphor was optimum when the concentration of Tb^{3+} was set to be 0.15 mol and the concentration of Eu^{3+} was set to be 0.22 mol. Under the accurate excitation of 373 nm near ultraviolet (n-UV) light, the emitting color of the phosphors can be tuned from green to red with increasing Eu^{3+}/Tb^{3+} ratio. It was further proved that the quadrupole–quadrupole (q–q) interaction is responsible for the energy transfer (ET) in the BLSOF:0.15Tb^{3+}, 0.22Eu^{3+} phosphor. Owing to the excellent thermal quenching luminescence property, the BLSOF:0.15Tb^{3+}, xEu^{3+} phosphor can be applied in n-UV white light emitting diodes (w-LEDs) and serve as the warm part of warm white light.

1. Introduction

Light emitting diodes (LEDs) have been used in a wide range of fields owing to their advantages, such as low-carbon emission, long service lifetime, high photoelectric conversion rate, environmentally-friendly performance, and so on.[1] The market for LEDs covers a variety of applications, for example, displays, traffic lights, decorative lighting and general lighting. In particular, white light emitting diodes (w-LEDs) have attracted the attention of researchers from all over the world, and have been called the fourth generation of lighting source owing to their outstanding merits in the general lighting field.[2–4] One method to produce w-LEDs capable of emitting high-quality white light is to combine tri-color phosphors with near ultraviolet (n-UV)-InGaN chips (350–420 nm).[5] In the applications of w-LEDs, several shortcomings of phosphor converted w-LEDs have been noted, such as low color rendering index (CRI), high correlated color temperature (CCT), blue light hazard induced by the former two, and different service lifetime of each part.[6,7] Long exposure to light of the blue and purple part of the spectrum can do harm to the retina, which is known as blue light hazard. The lack of a warm component in the light emitted by w-LEDs results in low CRI and high CCT. These studies highlight the importance of exploiting new kinds of phosphor to provide multicolor warm light in order to improve users' visual experience.[8–10]

Much recent research has focused on multicolor single-phase phosphors. Phosphors belonging to this category can avoid the drawbacks of inconsonant decay, inconsistent service lifetime and so on.[11] Generally, there are two methods to obtain multicolor single-phase phosphors: structure regulation, and energy transfer from sensitizer to activator.[12,13] There has been widespread application of energy transfer from sensitizers to activators, using an abundant range of host materials. Numerous sensitizer → activator ion pairs have been reported, including Eu^{2+} → Mn^{2+}, Tb^{3+} → Eu^{3+}, Ce^{3+} → Tb^{3+}, and so on.[14–16] Eu^{3+} can emit red light due to its electric dipole $^5D_0$ → $^7F_2$ transition, making it a suitable activator of the phosphor for w-LED requirements.[17–20] Terbium is usually used with europium to produce multicolor warm light, such as in $LaBWO_6$:Tb^{3+}, Eu^{3+}; Zn_2GeO_4:Tb^{3+}, Eu^{3+}; $Sr_3GdNa(PO_4)_3F$:Tb^{3+}, Eu^{3+}; $Sr_2Zr(PO_4)_6$:Tb^{3+}, Eu^{3+}; $KCaY(PO_4)_2$:Tb^{3+}, Eu^{3+} and so on.[21–25]

An appropriate activator and appropriate matrix are necessary to synthesize good phosphors. Outstanding photoluminescence can be achieved by doping rare earth (RE) elements in apatite. Apatite is a common choice for the matrix because of its good chemical stability and rich crystal field environment.[26] The general formula of apatite compounds can be expressed as $M_{10}(XO_4)_6Y_2$, in which M represents Ca, Sr, Ba, La, RE and so on; X represents Si, Ge, P and so on; Y represents F, Cl, Br, O and so on. It is widely known that there are two non-

[a]*Beijing Key Laboratory of Materials Utilization of Nonmetallic Minerals and Solid Wastes, National Laboratory of Mineral Materials, School of Materials Science and Technology, China University of Geosciences, Beijing 100083, China. E-mail: clayl@cugb.edu.cn; mlf@cugb.edu.cn; Fax: +86-10-82322974; +86-10-8232-1701; Tel: +86-10-82322039; +86-10-8233-1701*

[b]*School of Gemmology, China University of Geosciences, Beijing 100083, China*

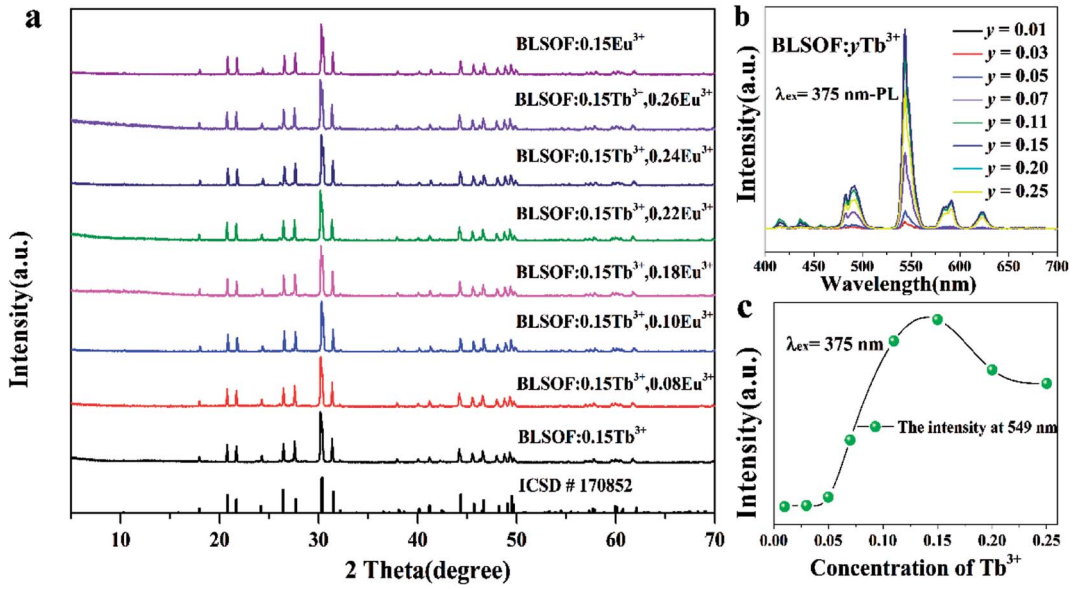

Fig. 1 (a) XRD patterns of BLSOF:0.15Tb^{3+}, BLSOF:0.15Eu^{3+} and BLSOF:0.15Tb^{3+}, $x$$Eu^{3+}$ phosphors. The standard data for BLSOF (ICSD No.170852) are also given as a reference. (b) The emission spectra of BLSOF:$y$$Tb^{3+}$ phosphors. (c) The concentration–intensity relationship of BLSOF:$y$$Tb^{3+}$ phosphors.

equivalent crystallographic sites in the apatite structure: the nine-coordinated 4f site with C_3 point symmetry and the seven-coordinated 6h site with C_s point symmetry, both of which are usually occupied by alkali metal, alkaline earth metal, and RE ions. Apatite compounds have been widely investigated for various applications, such as $Ca_9La(PO_4)_5(SiO_4)F_2$, $Sr_8La_2(PO_4)_6O_2$, $Ba_3LaK(PO_4)_3F$, and so on.[27–29] However, there is no report of the $Ba_2La_{3-x-y}Eu_xTb_y(SiO_4)_3F$(BLSOF:$Tb^{3+}$, Eu^{3+}) phosphor with apatite structure and oxyfluoride phase to the best of our knowledge.[30,31] In the crystal field environment of $Ba_2La_{3-x-y}Eu_xTb_y(SiO_4)_3F$, the La, Tb, and Eu ions should occupy the X sites, which include both 4f and 6h sites according to the theory mentioned above.

It is important to discover novel phosphors that can be excited by n-UV light (350–420 nm) to satisfy the needs of the market.[32] In this paper, the energy transfer mechanism in apatite compounds was investigated, and the performance of the studied phosphor under high temperature was found to be satisfactory. Under the accurate excitation of 373 nm n-UV light, the phosphor can emit light of different wavelengths depending on the doping ratio of Tb^{3+} and Eu^{3+}. It is concluded that the BLSOF:0.15Tb^{3+}, $x$$Eu^{3+}$ multicolor phosphor can be applied in n-UV w-LEDs and provide the warm part of warm light.

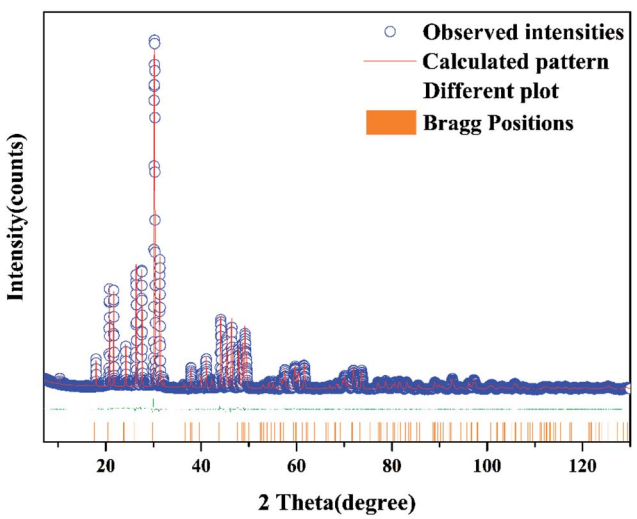

Fig. 2 Rietveld refinement XRD patterns of BLSOF at room temperature by TOPAS program. Solid red lines are calculated intensities, and blue circles are the observed intensities. Short vertical lines show the position of Bragg reflections of the calculated pattern. Green solid lines below the profiles stand for the difference between the observed and the calculated intensities.

2. Experimental details

2.1 Synthesis

The desired phosphors $Ba_2La_{2.85-x}Tb_{0.15}Eu_x(SiO_4)_3F$ were prepared *via* the conventional solid-state method under high

Table 1 Crystallographic data for BLSOF based on Rietveld refinement

Formula	$Ba_2La_3(SiO_4)_3F$
Space group	$P6_3/m$
Symmetry	Hexagonal
a/b (Å)	9.89093(21)
c (Å)	7.36654(19)
α/β	90°
γ	120°
V (Å^3)	624.120(32)
R-Bragg	3.42909
R_{exp} (%)	3.737
R_{wp} (%)	12.969
R_p (%)	9.280
χ^2	3.470

Table 2 The refined atomic positions and isotropic temperature factors for all atoms

Atoms	x	y	z	Occ	B_{eq}
La2	0.23946(23)	0.98545(25)	0.25	0.67(65)	1
Ba2	0.23946(23)	0.98545(25)	0.25	0.08(67)	1
Tb2	0.23946(23)	0.98545(25)	0.25	0.25(18)	1
La1	0.6666667	0.3333333	0.00082(56)	0.91(66)	1
Ba1	0.6666667	0.3333333	0.00082(56)	0.08(67)	1
Tb1	0.6666667	0.3333333	0.00082(56)	0.00(20)	1
Si1	0.4080(11)	0.37362(99)	0.25	1	1
O1	0.5970(24)	0.4536(22)	0.25	1	1
O2	0.3482(24)	0.5038(22)	0.25	1	1
O3	0.3557(13)	0.2672(13)	0.0697(16)	1	1
F	0	0	0.25	1	2.81

temperature. The raw materials included $BaCO_3$ (A.R.), La_2O_3 (99.99%), SiO_2 (A.R.), NH_4HF_2 (A.R.), Tb_4O_7 (99.99%) and Eu_2O_3 (99.99%), which were used directly without any other treatment. The selected starting materials were weighed according to the calculated precursor stoichiometry and mixed in an agate mortar. After thorough grinding, the stoichiometric mixture was transferred into an alumina crucible. The crucible was sealed into a high temperature tube furnace and annealed at 1350 °C for 5 h. After that, the sample was cooled to room temperature gradually, and ground into powder again for the series of tests that followed.

2.2 Characterization

XRD spectra were obtained on an X-ray powder diffractometer (XD-3, PGENERAL, China) with Cu-Kα radiation (λ = 0.15406 nm) operated at 40 kV and 30 mA. Powder diffraction data were fitted by the Rietveld method using the computer software TOPAS 3.0 package. PLE and PL spectra under room temperature were characterized on a Hitachi F-4600 fluorescence spectrophotometer. A PL system equipped with a xenon lamp (400 V, 150 W) acted as the excitation source. The thermal quenching luminescence properties were measured on the same spectrophotometer, which was combined with a self-made heating attachment and a computer-controlled electric furnace. A 400 nm cut off filter was applied in the experiment to remove the second-order emission of source radiation. Decay curves were monitored by an EDINBURGH FS5 Combined Fluorescence Lifetime & Steady State Spectrometer. Emission spectra of BLSOF:yTb^{3+} were measured on the same device with a 400 nm

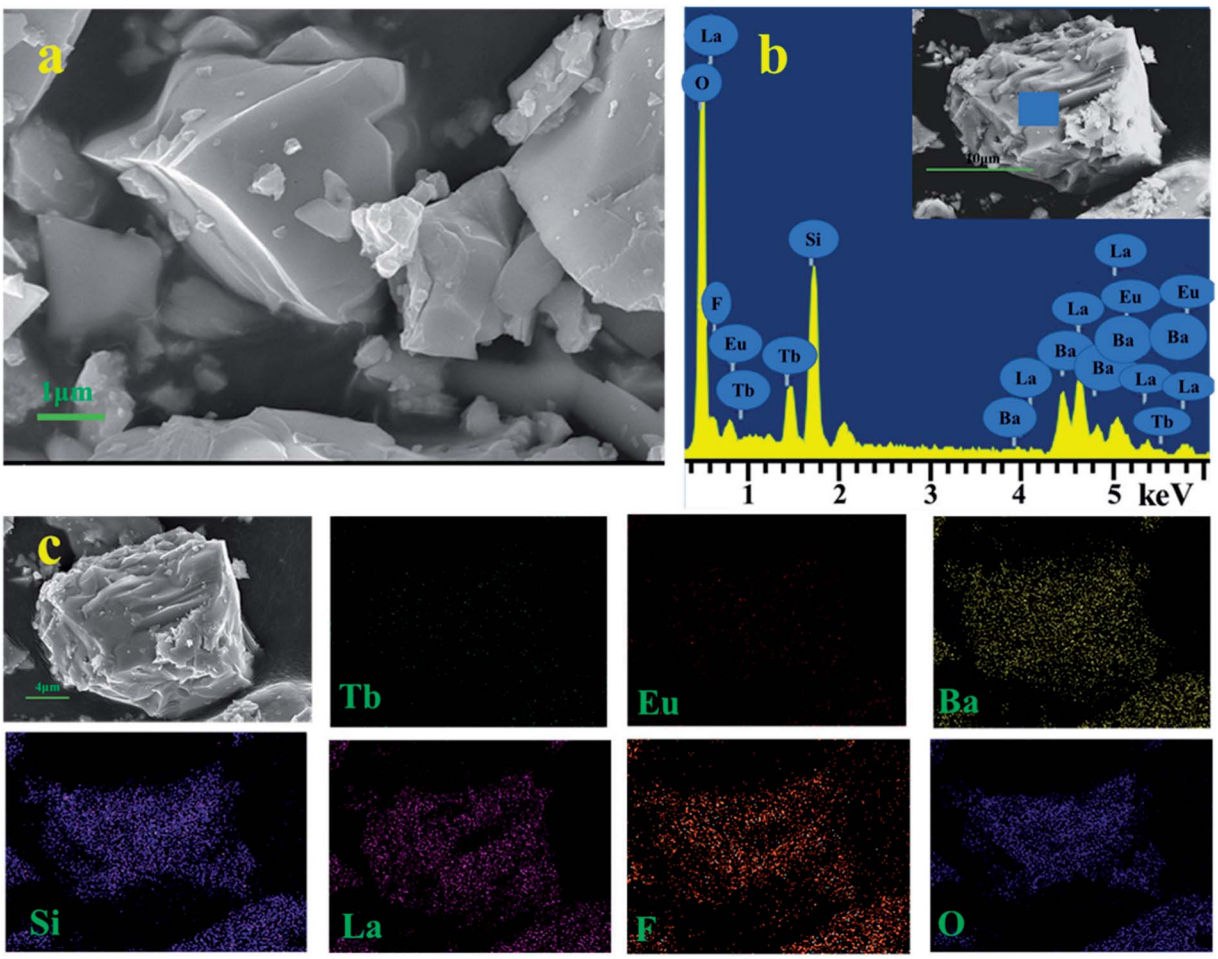

Fig. 3 (a) SEM image of BLSOF:0.15Tb^{3+}, 0.22Eu^{3+} phosphor. (b) EDX spectrum of BLSOF:0.15Tb^{3+}, 0.22Eu^{3+}. (c) Elemental mapping of BLSOF:0.15Tb^{3+}, 0.22Eu^{3+} phosphor.

cut off filter. Quantum yield was measured by an EDINBURGH FLS980 Spectrometer. Morphological analysis of the compounds was observed by SEM (JSM-6701F, Hitachi, Japan). Before the morphology was observed, the powder was coated on the conducting resin directly without any other measurement and sprayed with nano-platinum on the surface.

3. Results and discussions

Fig. 1(a) shows the typical XRD patterns of the as-prepared samples including the BLSOF:0.15Tb^{3+}, BLSOF:0.15Eu^{3+} and BLSOF:0.15Tb^{3+}, $x$$Eu^{3+}$ (x = 0.08, 0.1, 0.18, 0.22, 0.24, 0.26) phosphors. It is clear that the XRD peaks of the BLSOF phosphors can be accurately assigned to the phase of BLSOF (ICSD no. 170852), which belongs to the apatite structure with the hexagonal system and space group $P6_3/m$.[33] Fig. 1(b) shows the emission spectra of the BLSOF:$y$$Tb^{3+}$ phosphors and Fig. 1(c) shows the concentration–intensity relationship of the BLSOF:$y$$Tb^{3+}$ phosphors. The emission intensity reaches the maximum when the concentration of Tb^{3+} ions is 0.15 mol, above which the luminescence intensity decreases resulting from concentration quenching as widely noted in the literature.[34] Terbium ions act as the sensitizer and europium ions act as the activator in the BLSOF:Tb^{3+}, Eu^{3+} phosphors. When y = 0.15, the phosphor presents the strongest emission intensity. Considering this, the concentration of Tb^{3+} was fixed to be 0.15 mol and the concentration of Eu^{3+} was variable in the co-doped phosphors. In terms of their positions, the intensities of the diffraction peaks were matched perfectly with the reference ICSD file in Fig. 1(a). According to the substitution principle of isomorphism, Tb^{3+} and Eu^{3+} are assumed to replace La^{3+} in the structure and no charge compensation or vacancies will be formed as this is an isovalent substitution process. We can infer that the doping of Tb^{3+} and Eu^{3+} ions did not cause any structural change, which demonstrated that the isomorphic replacement of La^{3+} with Tb^{3+} and Eu^{3+} was successful in the present sample structure.[35]

Fig. 2 shows the Rietveld refinement of BLSOF:0.15Tb^{3+} at 298 K with λ = 1.5406 Å by the TOPAS program. The crystal structure of BLSOF (apatite-type structure) was taken as the starting model for Rietveld refinement and almost all peaks were indexed with parameters close to BLSOF. Solid red lines are the calculated intensities, and blue circles are the observed intensities. Short vertical lines show the position of Bragg reflections of the calculated pattern. Green solid lines below the profiles stand for the difference between the observed and the calculated intensities. Refinement was stable and gave low R-factors (Table 1, Fig. 2). All the experimental peaks were well fitted by the refinement, indicating that all of those peaks are Bragg reflections from the BLSOF structure and converge to R_{exp} = 3.737%, R_{wp} = 12.969%, R_p = 9.280% and χ^2 = 3.470. In the BLSOF compound, the lattice parameters are determined to be $a = b$ = 9.89093(21) Å, c = 7.36654(19) Å and V = 624.120(32) Å^3. The refined atomic positions and isotropic temperature factors for all atoms are also shown in Table 2.[36,37]

The microstructure of BLSOF:0.15Tb^{3+}, 0.22Eu^{3+} was determined and is shown in Fig. 3(a). The sample is composed of numerous smaller and larger blocks. The observation of Ba, La, Si, O, F, Tb, and Eu peaks in the EDX spectrum in Fig. 3(b) further implied the formation of the sample with the desired composition. In addition, the elemental mapping results as shown in Fig. 3(c) demonstrated that all the elements in the sample were homogeneously distributed throughout each block.[38]

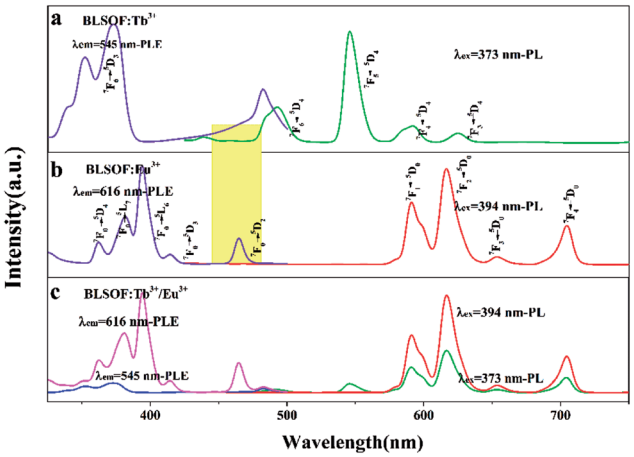

Fig. 4 (a) PLE spectrum (left) and PL spectrum (right) of BLSOF:0.15Tb^{3+}. (b) PLE spectrum (left) and PL spectrum (right) of BLSOF:0.15Eu^{3+}. (c) PLE spectrum (left) and PL spectrum (right) of BLSOF:0.15Tb^{3+}, 0.22Eu^{3+}.

The luminescence properties of the samples were studied in detail in the following work. The emission and excitation spectra of BLSOF:0.15Tb^{3+}, BLSOF:0.15Eu^{3+} and BLSOF:0.15Tb^{3+}, 0.22Eu^{3+} were measured. Fig. 4(a) depicts the spectra of the BLSOF:0.15Tb^{3+} phosphor. As shown in Fig. 4(a), the PLE spectrum of BLSOF:0.15Tb^{3+} shows typical excitation ranging from

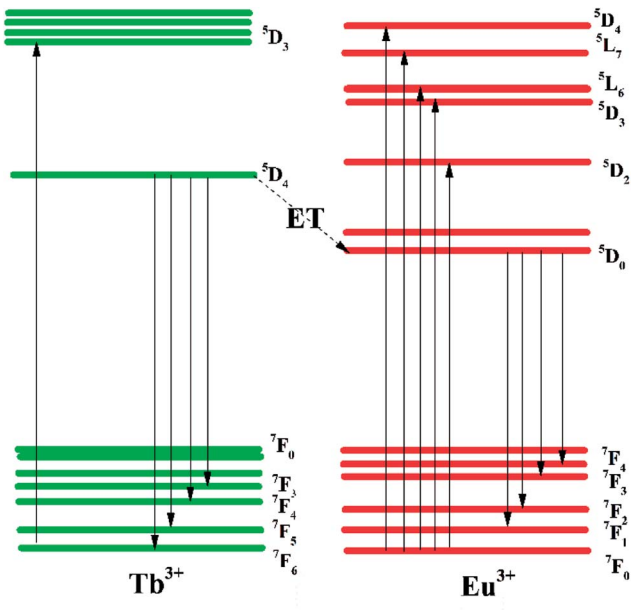

Fig. 5 The energy level transitions for PLE and PL of Tb^{3+} and Eu^{3+} and the corresponding energy level scheme of energy transfer from to Tb^{3+} to Eu^{3+}.

325 to 500 nm with a characteristic excitation peak at 373 nm ($^7F_6 \rightarrow {}^5D_3$), indicating that the excitation wavelength of the as-grown phosphors overlaps well with that of n-UV light LED chips. Upon 373 nm excitation, the phosphor emits sharp peaks of Tb^{3+} centered at 492, 545, 592 and 624 nm originating from transitions of $^5D_4 \rightarrow {}^7F_J$ ($J = 6, 5, 4, 3$). Fig. 4(b) depicts the spectra of the BLSOF:0.15Eu^{3+} phosphor. There are several peaks in these excitation spectra, which can be ascribed to transitions from the ground state $^7F_0$ to the excited states $^5D_4$ (362 nm), $^5L_7$ (381 nm), $^5L_6$ (394 nm), $^5D_3$ (414 nm), and $^5D_2$ (465 nm).[39,40] Upon 394 nm excitation, the BLSOF:0.15Eu^{3+} phosphor emits sharp peaks of Eu^{3+} centered at 591, 616, 654 and 700 nm originating from transitions of $^5D_0 \rightarrow {}^7F_J$ ($J = 1, 2, 3, 4$). Comparing Fig. 4(a) and (b), there is an overlap of the excitation spectrum of Eu^{3+} and emission spectrum of Tb^{3+} highlighted in yellow (about 445–485 nm), which means that energy transfer from Tb^{3+} to Eu^{3+} is possible in theory. Fig. 4(c) depicts the spectra of the BLSOF:0.15Tb^{3+}, 0.22Eu^{3+} phosphor. Using the same test parameters and coordinate range (in vertical and horizontal directions), PLE peaks at 373 nm, 394 nm and PL peaks at 545 nm, 616 nm were obtained and the relative intensity of the Tb^{3+} and Eu^{3+} peaks can be estimated from the spectra. Considering the excitation curves, the sample could be monitored by 616 nm and 545 nm, and excitation curve monitored by 616 nm is higher than the one monitored by 545 nm. Upon excitation, the sample shows emission from Eu^{3+} at an emission wavelength of 616 nm and from Tb^{3+} at an emission wavelength of 545 nm, and the former is more intense. The phosphor emits sharp peaks of Tb^{3+} and Eu^{3+} upon 373 nm excitation, which indicates that Tb^{3+}, Eu^{3+} co-doped BLSOFs can be used as green and red double-color emitting phosphors under n-UV excitation. Monitored at 394 nm, only red emission of Eu^{3+} could be observed, similar to the characteristic profile of the Eu^{3+} singly doped BLSOF sample. When the phosphor is excited by 373 nm, the peak of green curve at 616 nm is not as intense as the red curve (which was excited by 394 nm) in Fig. 4(c), indicating

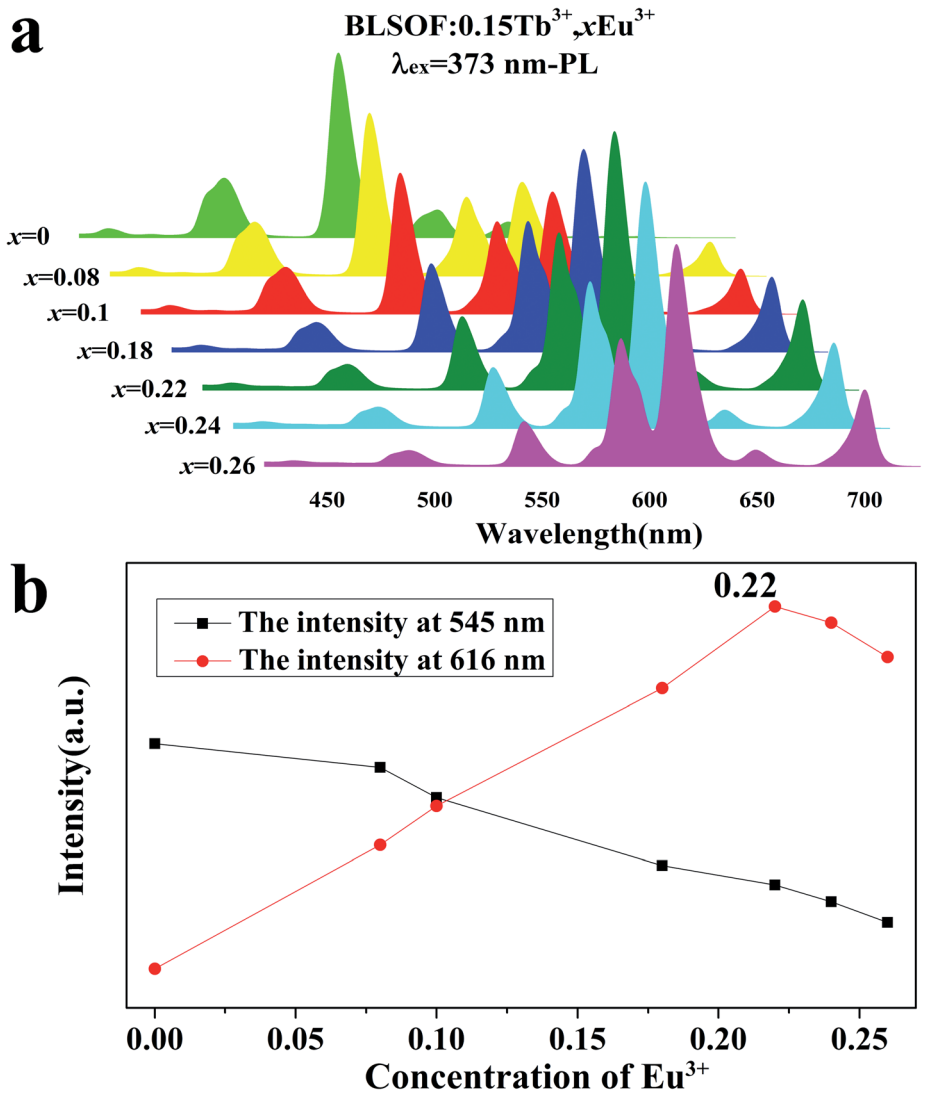

Fig. 6 (a) The PL spectra of BLSOF:0.15Tb^{3+}, xEu^{3+} phosphors ($x = 0$, 0.08, 0.1, 0.18, 0.22, 0.24 and 0.26) excited at 373 nm. (b) Emission intensity at 545 nm and 616 nm with various concentrations of europium.

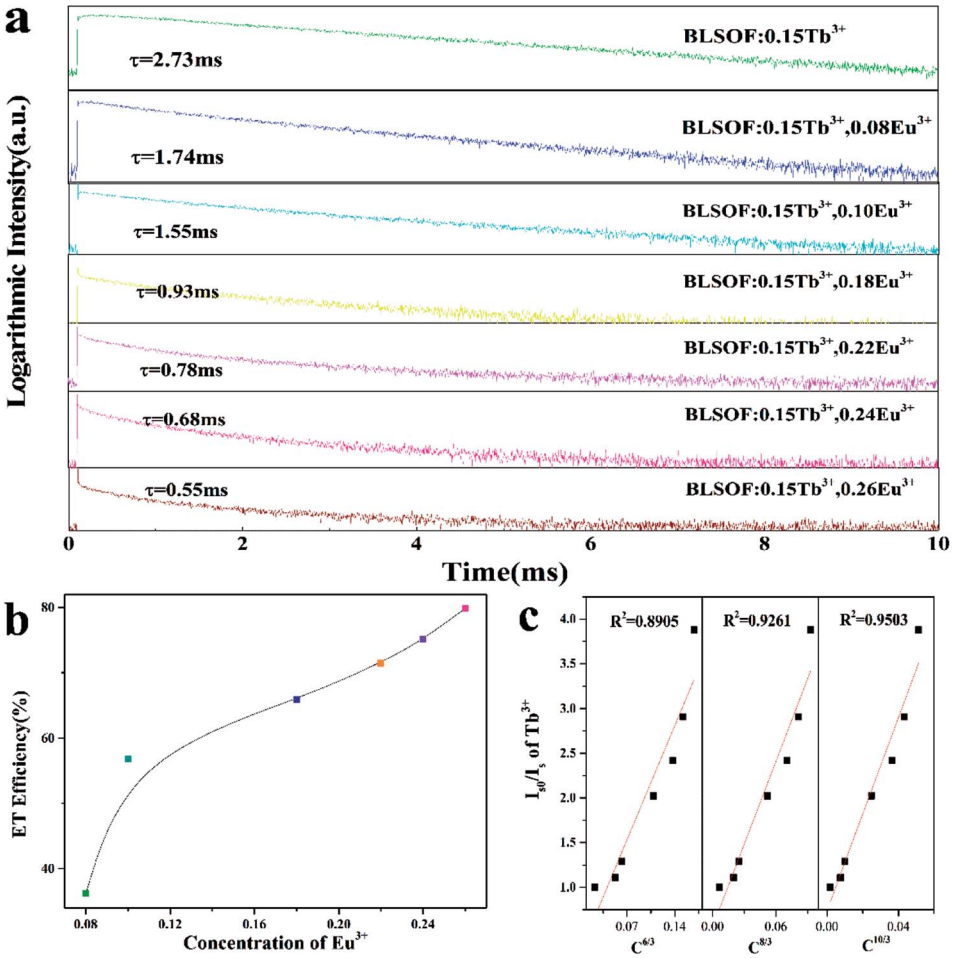

Fig. 7 (a) The luminescence decay curves of 545 nm emission in BLSOF:0.15Tb^{3+}, xEu^{3+} under the excitation of 373 nm. (b) The energy transfer efficiency of the phosphor under different concentrations of Eu^{3+}. (c) Dependence of I_{s0}/I_s of Tb^{3+} on $C^{6/3}$, $C^{8/3}$ and $C^{10/3}$.

a decrease in emission of Eu^{3+} at this excitation wavelength. The emission spectrum monitored at 373 nm includes not only the characteristic emission derived from Eu^{3+} ($^5D_0 \rightarrow {}^7F_2$ at 616 nm), but also the Tb^{3+} characteristic emission profile ($^5D_4 \rightarrow {}^7F_{6,5}$), similar to the Tb^{3+} singly doped sample. In this case, we focused on the emission spectra monitored at 373 nm to characterize the energy transfer properties from Tb^{3+} to Eu^{3+}. The results showed that the relative intensities of green and red emissions can be varied and multicolor emission may be achieved by adjusting the concentrations of Tb^{3+} and Eu^{3+} through energy transfer.[41]

An energy level diagram with all the relevant transitions is shown in Fig. 5 to visually illustrate the mechanism of luminescence and energy transfer. When the BLSOF:Tb^{3+}, Eu^{3+} phosphor is exposed to UV light, Tb^{3+} ions in the phosphor are excited from the ground state $^7F_6$ to the excited state $^5D_3$ and emit green light when they leap back from $^5D_4$ to ^7F_J (J = 6, 5, 4, 3) after non-radiative processes from $^5D_3$ to $^5D_4$. Energy transfer from the $^5D_4$ energy level of Tb^{3+} to the $^5D_0$ energy level of Eu^{3+} can also occur through a nonradiative process because the former is higher in energy. Furthermore, the Tb^{3+} emission curve, which is attributed to the transitions $^5D_4 \rightarrow {}^7F_{6,5,4,3}$, is greatly overlapped with the PLE curve of Eu^{3+}, which originates from the $^7F_0 \rightarrow {}^5D_{2,3}$ transition in Fig. 4. Red light is produced when Eu^{3+} ions return to the ground states $^7F_{1,2,3,4}$ through radiative transition.[42–44]

A series of PLE spectra of BLSOF:0.15Tb^{3+}, xEu^{3+} (x = 0, 0.08, 0.1, 0.18, 0.22, 0.24 and 0.26) under the excitation of 373 nm n-UV light are demonstrated in Fig. 6(a). The emission intensities at 545 and 616 nm with various concentrations of europium(x) are shown in Fig. 6(b). The emission intensity of Tb^{3+} (545 nm) continually decreases with increasing x and the emission intensity of Eu^{3+} (616 nm) ions first increases and then reaches the maximum when $x = 0.22$, after which the emission intensity decreases. Concentration quenching is the likely reason for the decrease in emission intensity above $x = 0.22$.[45] Thus, energy transfer occurs from Tb^{3+} to Eu^{3+} in BLSOF.[46]

To investigate the energy transfer mechanism, the decay curves of Tb^{3+} emission for $Ba_2La_{2.85-x}(SiO_4)_3F$:0.15$Tb^{3+}$, xEu^{3+} excited at 373 nm were characterized and are depicted in Fig. 7(a). The decay curves were fitted perfectly based on the following single exponential decay equation:[47]

$$I(t) = I_0 + A\exp(-t/\tau) \quad (1)$$

where I and I_0 are the luminescence intensity at time t and 0, A is constant, t is the time, and τ is the decay time for the

component. The decay curves of BLSOF:0.15Tb^{3+}, xEu^{3+} compounds monitored at 545 nm with 373 nm excitation are shown in Fig. 7(a). The lifetime of Tb^{3+} decreased gradually with the increasing concentration of Eu^{3+}, further confirming the existence of energy transfer from Tb^{3+} to Eu^{3+} in BLSOF. The energy transfer efficiency from Tb^{3+} to Eu^{3+} can be calculated based on the following expression:[48]

$$\eta = 1 - (\tau_s/\tau_{s0}) \quad (2)$$

where τ_{s0} and τ_s are the corresponding lifetimes of donor Tb^{3+} in the absence and presence of the acceptor Eu^{3+}. As shown in Fig. 7(b), the η value is estimated to be 36.26%, 56.78%, 65.93%, 71.43%, 75.09% and 79.85% when the concentration of Eu^{3+} is 0.08, 0.10, 0.18, 0.22, 0.24 and 0.26 mol. Clearly, the energy transfer efficiency increases as the concentration of Eu^{3+} increases. Furthermore, the internal quantum yield for Tb^{3+} and Eu^{3+} is measured to be 24.04%, 53.52%, 66.89%, 53.11%, and 31.78% when the concentration of Eu^{3+} is 0, 0.08, 0.10, 0.18, and 0.22 mol.

It is well-known that the mechanism of nonradiative energy transfer among the dopants can be either exchange interaction or electric multipolar interaction. Which of these applies in a particular case can be confirmed by analyzing the critical distance. Based on Blasse's theory, the critical distance R_c can be estimated by using the following equation:[49–53]

$$R_c \approx 2(3V/4\pi x_c N)^{1/3} \quad (3)$$

where V stands for the volume of the unit cell, x_c is the total concentration of sensitizer Tb^{3+} and activator Eu^{3+}, and N represents the number of host cations in one unit cell. For the $Ba_2La_3(SiO_4)_3F$ host, the analytical and experimental values were $N = 10$, $V = 608.77$ Å^3, and the critical value of x_c is about 0.246, *i.e.* the total concentration of Tb^{3+} and Eu^{3+} at which the ET efficiency is 0.5. Therefore, the R_c of BLSOF:0.15Tb^{3+}, xEu^{3+} was determined to 7.789 Å. In general, when the critical distance is no larger than 5 Å, the exchange interaction contributes to the concentration quenching mechanism. Otherwise, the electric multipolar interaction prevails. Thus, the electric multipolar interaction is the mechanism of the nonradiative energy transfer from Tb^{3+} to Eu^{3+} in BLSOF.

Additionally, Fig. 7(c) shows the dependence of I_{s0}/I_s of Tb^{3+} on $C^{6/3}$, $C^{8/3}$ and $C^{10/3}$ (C is the total concentration of Tb^{3+} and Eu^{3+}). On the basis of Dexter's energy transfer formula of multipolar interactions, the following relationship can be given:[54,55]

$$(\eta_0/\eta_s) \propto C^{n/3} \quad (4)$$

where η_0/η_s is the ratio of the quantum efficiencies of Tb^{3+} in the absence and presence of Eu^{3+}, C is the total concentration of Tb^{3+} and Eu^{3+}, and n is a constant which indicates the interaction between Tb^{3+} and Eu^{3+} ($n = 6$, dipole–dipole interaction; $n = 8$, dipole–quadrupole interaction; and $n = 10$, quadrupole–quadrupole interaction). The value of η_0/η_s can be approximately calculated by the ratio of the two related luminescence intensities (I_{s0}/I_s) according to the formula (1):[56]

Table 3 CIE value of BLSOF:0.15Tb, xEu^{3+} ($x = 0$, 0.08, 0.1, 0.18, 0.22, 0.24, 0.26), BLSOF:0.15Eu^{3+} samples

Number	Formula	CIE value
1	$Ba_2La_{2.85}(SiO_4)_3F$:0.15Tb^{3+}	(0.2908, 0.5282)
2	$Ba_2La_{2.77}(SiO_4)_3F$:0.15Tb^{3+}, 0.08Eu^{3+}	(0.4083, 0.4652)
3	$Ba_2La_{2.75}(SiO_4)_3F$:0.15Tb^{3+}, 0.10Eu^{3+}	(0.4397, 0.4445)
4	$Ba_2La_{2.67}(SiO_4)_3F$:0.15Tb^{3+}, 0.18Eu^{3+}	(0.5160, 0.4027)
5	$Ba_2La_{2.63}(SiO_4)_3F$:0.15Tb^{3+}, 0.22Eu^{3+}	(0.5413, 0.3872)
6	$Ba_2La_{2.61}(SiO_4)_3F$:0.15Tb^{3+}, 0.24Eu^{3+}	(0.5454, 0.3802)
7	$Ba_2La_{2.59}(SiO_4)_3F$:0.15Tb^{3+}, 0.26Eu^{3+}	(0.5534, 0.3745)
8	$Ba_2La_{2.85}(SiO_4)_3F$:0.15Eu^{3+}	(0.6125, 0.3314)

$$(I_{s0}/I_s) \propto C^{n/3} \quad (5)$$

where I_{s0} and I_s are the intrinsic luminescence intensities of Tb^{3+} in the absence and presence of Eu^{3+}. Plots of the value of I_{s0}/I_s and $C^{n/3}$ ($n = 6$, 8, or 10) are depicted in Fig. 7(c). It can be easily observed that a highly linear relationship between I_{s0}/I_s and $C^{n/3}$ occurs when $n = 10$, implying that the energy transfer from Tb^{3+} to Eu^{3+} occurs *via* a quadrupole–quadrupole mechanism.[57]

The color coordinates of the BLSOF:0.15Tb^{3+}, xEu^{3+} phosphors under the excitation of 373 nm were calculated and are presented in Table 3 and Fig. 8. The chromaticity coordinates (x, y) of BLSOF:0.15Tb^{3+}, xEu^{3+} were calculated based on the corresponding emission spectra. In order to be more intuitive, digital photographs of BLSOF:0.15Tb^{3+}, BLSOF:0.15Tb^{3+}, 0.08Eu^{3+}, BLSOF:0.15Tb^{3+}, 0.22Eu^{3+} and BLSOF:0.15Eu^{3+} upon 365 nm UV-lamp excitation are given in the insets of Fig. 8. The series of phosphors were able to be tuned from green (0.29, 0.53), through

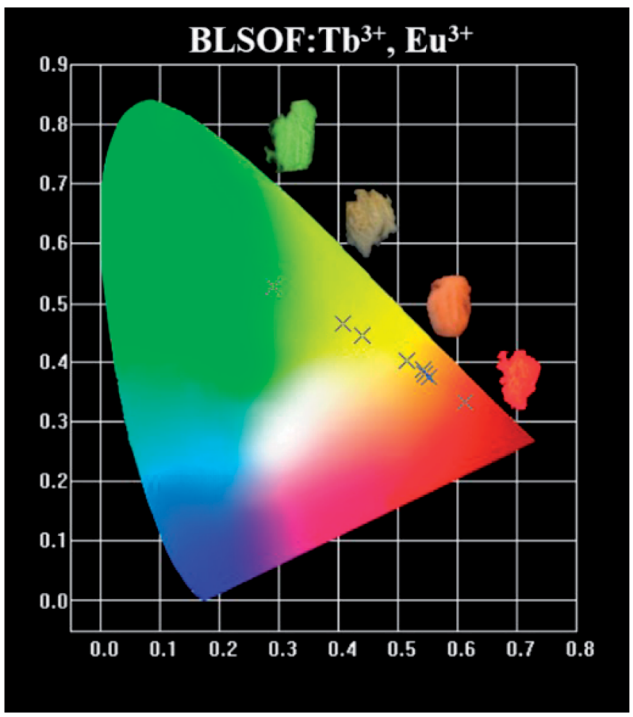

Fig. 8 The CIE value of BLSOF:0.15Tb^{3+}, xEu^{3+} under the excitation of 373 nm.

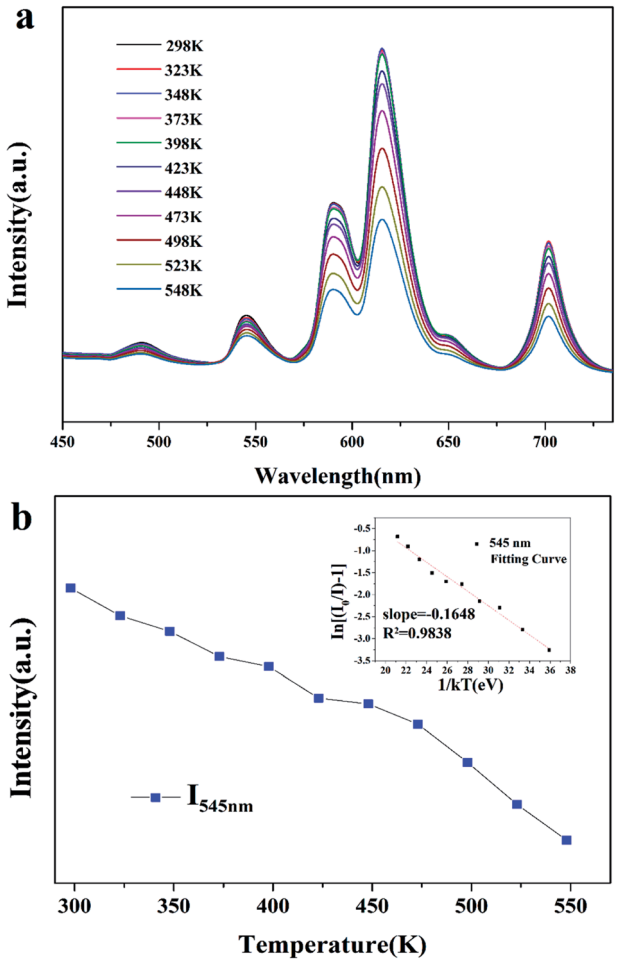

Fig. 9 (a) Temperature-dependent luminescence of BLSOF:0.15Tb^{3+}, 0.22Eu^{3+}. (b) Temperature–intensity dependence of BLSOF:0.15Tb^{3+}, 0.22Eu^{3+} and the inset shows $\ln(I_0/I - 1)$ *versus* $1/kT$ for the BLSOF:0.15Tb^{3+}, 0.22Eu^{3+} sample.

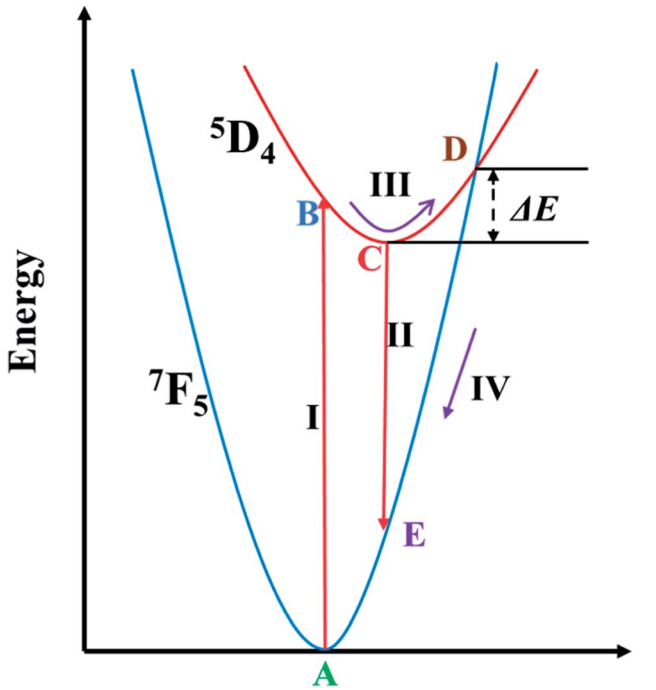

Fig. 10 Configurational coordinate diagram showing the thermal quenching process for Tb^{3+} ions.

yellow/orange-red to red (0.61, 0.33) by adjusting the proportion of Tb^{3+} and Eu^{3+} concentrations. The results indicate that the prepared phosphors show the merit of multicolor emissions in the visible region when excited by a single wavelength of light, which means that tunable luminescence can be realized in the novel BLSOF:0.15Tb^{3+}, xEu^{3+} phosphors based on energy transfer.[58–60]

As is well known, the thermal stability of coated phosphors has a critical influence on the performance of LEDs. Fig. 9(a) shows the temperature-dependent emission spectra for the BLSOF:0.15Tb^{3+}, 0.22Eu^{3+} phosphor and Fig. 9(b) shows the intensity–concentration relationship of Tb^{3+} ($^5D_4 \rightarrow {}^7F_5$) at 545 nm. It can be seen that the luminescence intensity at 150 °C remains 85.34% of that at room temperature, 25 °C. To understand the temperature-dependent thermal quenching behavior, the activation energy was calculated, as shown in the inset of Fig. 9(b), by means of the following formula:

$$\ln(I_0/I - 1) = \ln A - \Delta E/kT \quad (6)$$

where I_0 stands for initial emission intensity, I corresponds to the emission intensity at different temperatures, A is the coefficient, ΔE means the activation energy, k is the Boltzmann coefficient with a fixed value of 8.629×10^{-5} eV K^{-1} and T is the temperature. The inset of Fig. 9(b) shows the plot of $\ln(I_0/I - 1)$ *vs.* $1/kT$ for the BLSOF:0.15Tb^{3+}, 0.22Eu^{3+} sample. As demonstrated, the experimental data were linearly fitted with a slope of approximately −0.1648, suggesting that the activation energy for thermal quenching of the Tb^{3+} ions in the BLSOF:0.15Tb^{3+}, 0.22Eu^{3+} sample is 0.1648 eV.[61]

The configuration coordinate diagram for the $^7F_5 \rightarrow {}^5D_4$ (545 nm) transition of Tb^{3+} is shown in Fig. 10 to make the thermal quenching process clearer. When the phosphor was exposed to 373 nm light, the electrons of Tb^{3+} could be pumped from point A in the $^7F_5$ level to point B in the $^5D_4$ level as process I, and then non-radiatively relax to point C, and leap back to point E in the $^7F_5$ level and give out light as process II. The $^7F_5$ and $^5D_4$ states overlapped at point D, and ΔE is the energy difference between D and C. For this phosphor, the energy difference was calculated to be 0.1648 eV as above. At high temperature, the centers will be thermally activated from point B to the junction of point D, corresponding to process III, and then non-radiatively relax to point A as process IV. The higher the temperature, the more electrons can overcome the activation energy. As a result, thermal quenching phenomena occur and the emission intensity of Tb^{3+} decreases with increasing temperature.[62,63]

4. Conclusions

In summary, a multicolor warm phosphor, BLSOF:0.15Tb^{3+}, xEu^{3+}, was synthesized by the traditional high-temperature solid-state method. The results reveal that the color of the BLSOF:0.15Tb^{3+}, xEu^{3+} phosphors can be modulated from

green, through yellow/red-orange to red with different Tb^{3+}/Eu^{3+} ratios. The chromaticity coordinates of the BLSOF:0.15Tb^{3+}, xEu^{3+} phosphors gradually shift from green (0.29, 0.53) through yellow/red-orange and eventually to red (0.61, 0.33) with increasing Eu^{3+} concentration. Based on Dexter's energy transfer equation, the quadrupole–quadrupole interaction (q–q) is responsible for the energy transfer from Tb^{3+} to Eu^{3+} in BLSOF. The energy level diagram with all the relevant transitions and the configuration coordinate diagram have also been discussed to make the luminescence and thermal quenching process easier to understand. The properties of this phosphor are also stable under high temperature and the applicability of this phosphor is greatly enhanced, suggesting its promising potential. All the observed features indicate that the multicolor phosphor might be a good candidate as a single-phase warm emitter for warm w-LEDs.

Conflicts of interest

There are no conflicts to declare.

Acknowledgements

This present work is supported by the National Natural Science Foundations of China (Grant No. 51672257, 41672044 and 41172053), and the Fundamental Research Funds for the Central Universities (Grant No. 2652017091 and 2652017370).

References

1 S. Ray, P. Tadge, S. Dutta, T. M. Chen, G. B. Nair and S. J. Dhoble, *Ceram. Int.*, 2018, **44**, 8334–8343.
2 X. Y. Huang and H. Guo, *RSC Adv.*, 2018, **8**, 17132–17138.
3 B. Li, Q. Sun, S. Y. Wang, H. Guo and X. Y. Huang, *RSC Adv.*, 2018, **8**, 9879–9886.
4 Z. Li, Q. L. Pian, L. Li, Y. Sun and S. S. Zheng, *Optik*, 2018, **161**, 38–43.
5 Z. M. Wang, J. Zou, C. Y. Zhang, B. B. Yang, M. M. Shi, Y. Li, H. Y. Zhou, Y. M. Liu, M. T. Li and Z. Z. Liu, *J. Non-Cryst. Solids*, 2018, **489**, 57–63.
6 G. C. Hu, X. Hu, W. Chen, Y. Z. Cheng, Z. C. Liu, Y. J. Zhang, X. J. Liang and W. D. Xiang, *Mater. Res. Bull.*, 2017, **95**, 277–284.
7 P. Fulmek, J. Nicolics, W. Nemitz and F. P. Wenzl, *Mater. Chem. Phys.*, 2017, **196**, 82–91.
8 J. Liu, G. Li, H. J. Guo, D. W. Liu, P. Feng and Y. H. Wang, *RSC Adv.*, 2018, **8**, 10246–10254.
9 B. C. Wang, Y. G. Liu, Z. H. Huang and M. H. Fang, *RSC Adv.*, 2018, **8**, 15587–15594.
10 D. Kim, S. Park, B. C. Choi, S. H. Park, J. H. Jeong and J. H. Kim, *Mater. Res. Bull.*, 2018, **97**, 115–120.
11 J. M. Xiang, J. Y. Chen, N. M. Zhang, H. B. Yao and C. F. Guo, *Dyes Pigm.*, 2018, **154**, 257–262.
12 H. K. Liu, L. B. Liao, Y. Y. Zhang, T. S. Zhou, Q. F. Guo, L. Li and L. F. Mei, *Dyes Pigm.*, 2017, **140**, 87–91.
13 Q. F. Guo, L. B. Liao and Z. G. Xia, *J. Lumin.*, 2014, **145**, 65–70.
14 Z. Y. Mao, J. J. Chen, J. Li and D. J. Wang, *Chem. Eng. J.*, 2016, **284**, 1003–1007.
15 S. L. Yuan, L. T. Wang, Y. X. Yang, F. Cheviré, F. Tessier and G. R. Chen, *Ceram. Int.*, 2016, **42**, 12508–12511.
16 K. Li, H. Z. Lian, Y. Q. Han, M. M. Shang, R. Van Deun and J. Lin, *Dyes Pigm.*, 2017, **139**, 701–707.
17 X. Min, Y. K. Sun, L. T. Kong, M. Guan, M. H. Fang, Y. G. Liu, X. W. Wu and Z. H. Huang, *Dyes Pigm.*, 2018, **157**, 47–54.
18 M. F. Xia, Z. H. Ju, H. Yang, Z. B. Wang, X. P. Gao, F. X. Pan and W. S. Liu, *J. Alloys Compd.*, 2018, **739**, 439–446.
19 S. Kaur, M. Jayasimhadri and A. S. Rao, *J. Alloys Compd.*, 2017, **697**, 367–373.
20 J. S. Zhong, H. B. Gao, Y. J. Yuan, L. F. Chen, D. Q. Chen and Z. G. Ji, *J. Alloys Compd.*, 2018, **735**, 2303–2310.
21 B. Li, X. Y. Huang, H. Guo and Y. J. Zeng, *Dyes Pigm.*, 2018, **150**, 67–72.
22 Q. Y. Bai, Z. J. Wang, P. L. Li, S. C. Xu, T. Li, J. G. Cheng and Z. P. Yang, *Mater. Des.*, 2016, **108**, 597–607.
23 N. Guo, Q. M. Liang, S. Li, R. Z. Ouyang and W. Lü, *Opt. Mater.*, 2017, **73**, 570–576.
24 Y. M. Feng, J. P. Huang, C. M. Li, G. Hu, J. Liu and X. B. Yu, *J. Alloys Compd.*, 2017, **706**, 478–484.
25 X. G. Zhang, L. Y. Zhou, J. X. Shi and M. L. Gong, *Mater. Lett.*, 2014, **137**, 32–35.
26 Y. Y. Zhang, L. F. Mei, H. K. Liu, D. Yang, L. B. Liao and Z. H. Huang, *Dyes Pigm.*, 2017, **139**, 180–186.
27 H. Guo, B. Devakumar, B. Li and X. Y. Huang, *Dyes Pigm.*, 2018, **151**, 81–88.
28 H. K. Liu, Y. Y. Zhang, L. B. Liao, Q. F. Guo and L. F. Mei, *Ceram. Int.*, 2014, **40**, 13709–13713.
29 X. X. Ma, L. F. Mei, H. K. Liu, L. B. Liao, K. Nie, Y. Q. Liu and Z. H. Li, *Polyhedron*, 2016, **119**, 223–226.
30 P. Hagenmuller, *J. Phys. Chem. Solids*, 1998, **59**, 503–506.
31 P. Hagenmuller, *J. Power Sources*, 2000, **90**, 9–12.
32 B. Wang, A. Q. Zhang, X. F. Yang, Q. Wang, Q. Q. Shen, X. G. Liu and H. S. Jia, *J. Alloys Compd.*, 2017, **729**, 117–125.
33 M. Runowski, S. Goderski, J. Paczesny, M. Księżopolska-Gocalska, A. Ekner-Grzyb, T. Grzyb, J. D. Rybka, M. Giersig and S. Lis, *J. Phys. Chem. C*, 2016, **120**, 23788–23798.
34 R. J. Yu, J. Wang, M. Zhang, J. H. Zhang, H. B. Yuan and Q. Su, *Chem. Phys. Lett.*, 2008, **453**, 197–201.
35 M. Runowski and S. Lis, *J. Alloys Compd.*, 2014, **597**, 63–71.
36 A. Durugkar, S. Tamboli, N. S. Dhoble and S. J. Dhoble, *Mater. Res. Bull.*, 2018, **97**, 466–472.
37 Y. Guo, B. K. Moon, B. C. Choi, J. H. Jeong, J. H. Kim and H. Choi, *Ceram. Int.*, 2016, **42**, 18324–18332.
38 P. Du, X. Y. Huang and J. S. Yu, *Chem. Eng. J.*, 2018, **337**, 91–100.
39 H. Guo, X. Y. Huang and Y. J. Zeng, *J. Alloys Compd.*, 2018, **741**, 300–306.
40 K. Binnemans, *Coord. Chem. Rev.*, 2015, **295**, 1–45.
41 X. M. Zhu and Z. F. Zhou, *J. Lumin.*, 2017, **188**, 589–594.
42 Z. Chen, X. A. Chen, S. M. Huang and Y. X. Pan, *Ceram. Int.*, 2016, **42**, 13476–13484.
43 H. Guo, B. Devakumar, B. Li and X. Y. Huang, *Dyes Pigm.*, 2018, **151**, 81–88.

44 A. G. Bispo-Jr, S. A. M. Lima and A. M. Pires, *J. Lumin.*, 2018, **199**, 372–378.
45 H. Jing, C. F. Guo, G. G. Zhang, X. Y. Su, Z. Yang and J. H. Jeong, *J. Mater. Chem.*, 2012, **22**, 13612–13618.
46 N. Guo, C. Z. Jia, J. Li, Y. F. Zhao, R. Z. Ouyang and W. Lü, *J. Am. Ceram. Soc.*, 2015, **98**, 1162–1168.
47 P. Du, Z. G. Xia and L. B. Liao, *J. Lumin.*, 2013, **133**, 226–229.
48 H. K. Liu, Q. F. Guo, L. B. Liao and Z. G. Xia, *Opt. Commun.*, 2013, **309**, 64–67.
49 L. Qin, P. Q. Cai, C. L. Chen, J. Wang, S. I. Kim, Y. L. Huang and H. J. Seo, *J. Alloys Compd.*, 2018, **738**, 372–378.
50 J. Zhao, C. F. Guo, T. Li, X. Y. Su, N. M. Zhang and J. Y. Chen, *Dyes Pigm.*, 2016, **132**, 159–166.
51 P. Du, Z. G. Xia and L. B. Liao, *Mater. Res. Bull.*, 2011, **46**, 543–546.
52 G. Blasse, *Phys. Lett. A*, 1968, **28**, 444–445.
53 G. Blasse, *J. Solid State Chem.*, 1986, **62**, 207–211.
54 Q. F. Guo, L. B. Liao, L. F. Mei and H. K. Liu, *J. Solid State Chem.*, 2015, **232**, 102–107.
55 Q. F. Guo, L. B. Liao, L. F. Mei, H. K. Liu and Y. Hai, *J. Solid State Chem.*, 2015, **225**, 149–154.
56 S. A. Khan, W. W. Ji, L. Y. Hao, X. Xu, S. Agathopoulos and N. Z. Khan, *Opt. Mater.*, 2017, **72**, 637–643.
57 K. Li, D. L. Geng, M. M.Shang, Y. Zhang, H. Z. Lian and J. Lin, *J. Phys. Chem. C*, 2014, **118**, 11026–11034.
58 X. Chen, P. P. Dai, X. T. Zhang, C. Li, S. Lu, X. L. Wang, Y. Jia and Y. C. Liu, *Inorg. Chem.*, 2014, **53**, 3441–3448.
59 Z. G. Xia and Q. L. Liu, *Prog. Mater. Sci.*, 2016, **84**, 59–117.
60 R. Zhang, B. Y. Wang, P. Zhou, X. L. Wu, X. H. Huang and B. Wang, *Mater. Lett.*, 2018, **221**, 31–34.
61 L. F. Mei, J. Xie, H. K. Liu, L. B. Liao, Y. Y. Zhang and M. L. Li, *Opt. Commun.*, 2015, **335**, 90–93.
62 S. Mahlik, F. Diaz and P. Boutinaud, *J. Lumin.*, 2017, **191**, 18–21.
63 H. Ye, M. Y. He, T. S. Zhou, Q. F. Guo, J. L. Zhang, L. B. Liao, L. F. Mei, H. K. Liu and M. Runowski, *J. Alloys Compd.*, 2018, **757**, 79–86.